Full paper

A multifunctional robotic system toward moveable sensing and energy harvesting

Yiqiang Fu [a,b,c], Hongqiang Wang [a,b,d,e,*], Yunlong Zi [c,**], Xuanquan Liang [a,b]

[a] *Shenzhen Key Laboratory of Biomimetic Robotics and Intelligent Systems, Department of Mechanical and Energy Engineering, Southern University of Science and Technology, Shenzhen, Guangdong 518055, China*
[b] *Guangdong Provincial Key Laboratory of Human-Augmentation and Rehabilitation Robotics in Universities, Southern University of Science and Technology, Shenzhen, Guangdong 518055, China*
[c] *Department of Mechanical and Automation Engineering, The Chinese University of Hong Kong, Shatin, NT, Hong Kong, China*
[d] *Southern Marine Science and Engineering Guangdong Laboratory, Guangzhou, Guangdong, China*
[e] *State Key Laboratory of Robotics, Shenyang Institute of Automation, Chinese Academy of Sciences, Shenyang 110016, China*

ARTICLE INFO

ABSTRACT

The operations of the triboelectric nanogenerator (TENG) highly rely on the availability of the mechanical motion source depending on the location, time, weather, etc. Thus, it is highly demanded to achieve moveable mechanical sensing and energy harvesting, but it is also challenging considering the system complexity, size, and weight. To this end, an electrostatic robotic system capable of locomotion, energy harvesting, and vibration sensing is proposed in this paper. The main body of the robot is an integration of an electrostatic actuator and a TENG, both of which share the same structure and materials and utilize the mechanical and electrical characteristics of electrostatic effects, respectively. The prototype is lightweight (2.46 g) and compact (3.7 cm in height and 9.1 cm in length), consisting of two conductive films as the main body in a zipper-like form and two flat conductive films as feet. Here we demonstrate the multifunctionality of this prototype by driving the robot crawling on the ground at a speed of 2.2 mm/s at maximum with a mini camera for monitoring, anchoring by electrostatic adhesive feet at the aim location where vibration is strong, sensing the vibration frequency accurately while having an average relative error of 8.7% in measuring the amplitude, and harvesting the energy by TENG. Such a multifunctional robotic system may enable broad potential applications in structural health monitoring, environmental surveillance, rescue, risky intervention, etc.

1. Introduction

Nowadays, enormous widely distributed sensor nodes are placed in every corner of the world to satisfy the rapid development of the Internet of Things (IoT), smart city, and big data [1]. Mechanical motions such as machine vibrations, wind-structure interactions, water wave oscillations, etc., which are abundant in the environment [2], can become potential sensing sources for monitoring purpose, as well as sustainable energy sources for powering sensor nodes. However, the availability of mechanical motions usually highly depends on the location, time, and weather. Thus, the relocation of the sensing or energy harvesting devices is frequently demanded, which raises a challenge for the continuous operations of these devices. Moveable sensors and energy harvesters are

highly desired to capture the mechanical signals and energy sources successively. Robotic technology provides a possible solution to address the demands of relocation of the devices. Although promising, the integration of robotics, sensors, and energy harvesters faces grand challenges on both the actuation and sensing aspects, concerning the system complexity, size, and weight.

Traditional mechanical sensing and mechanical energy harvesting rely on either electromagnetic generators (EMG) or piezoelectric energy harvesters (PEH) [3–5]. EMGs require magnets and wire coils, which are usually heavy and bulky [6], and thus it is not easy to be carried by robots. PEHs usually require additional structures to trigger their high dynamic performance [7], which also brings difficulties in installation and maintenance to be integrated into robots. With the emerging

---

technology of the triboelectric nanogenerator (TENG) [8], high-performance mechanical energy harvesting [9,10] and self-powered sensing [11,12] have been demonstrated since 2012 with advantages of simple structure, lightweight, low cost, and facile fabrication [13]. Moreover, TENGs have been demonstrated to have great compatibility with actuators and robots in terms of supplying power [14, 15]. The study of TENGs has been ongoing for almost a decade, yet none of the proposed TENGs can achieve moveable energy harvesting, let alone movable vibration sensing. Conventionally, the mobility is enabled by employing actuators or motors, which, however, can make the TENG bulky and high-cost. Sun et al. [14] used a freestanding mode TENG to power a robot that is based on a unidirectional dielectric elastomer actuator (DEA). It might be the first combination of a TENG with a DEA, but the role of the TENG is just a battery, not even a moveable one (portable by the robot). A similar case can be seen in Ref. [10] on the study of a triboelectric micromotor. To achieve moveable energy harvesting and even moveable vibration sensing, TENG has to be integrated with a suitable robotic actuation mechanism.

On the aspect of robotic actuation, the electrostatic actuator [16,17] becomes a good match. The electrostatic robot, which utilizes the electrostatic forces to provide power for locomotion, has been rapidly developed in recent years [18–21]. A typical electrostatic actuator is composed of only two conductive foils and an insulation layer between the conductors [18]. It possesses various advantageous features including being lightweight, low-profile, compliant, and quick in response [22], compared with the conventional electromagnetic motors, piezoelectric actuators, and shape memory alloys [23]. Moreover, it is intrinsically a good match for TENGs, since they are both based on the electrostatic field and share a similar structure of conductive foils and insulation layers. Electrostatic robots can serve as the ideal carrier of TENGs to enable moveable sensing and energy harvesting. In the meanwhile, the signals collected by sensors may contribute information for the decision-making of the intelligent robotic systems, and the energy harvested may provide an additional power supply for the robotics. Besides, Multifunctionality is commonly required in robotics and is usually directly achieved by employing different functional modules. However, these additional modules can be fatal to small soft robots, resulting in reduced flexibility, increased weight, incompact structure, etc. Therefore, enabling multifunctionality at the lowest cost is absolutely vital and has been one of the most active research topics in robotics.

In this work, we design a zipper-like robotic system integrating a TENG for sensing and energy harvesting and an electrostatic actuator for robotic actuation. This mesoscale robot measures 3.7 cm in height and 9.1 cm in length. Since multiple functions of sensing, energy harvesting, and locomotion are achieved through shared electrodes and structures, this robot weighs only 2.46 g. It can travel with 2.2 mm/s at maximum on the ground with the electrostatic actuators. After moving to the aim location, the robot becomes a sensor, which can accurately identify the vibration frequency with low relative errors (below 20%) in measuring the vibration amplitude, or an energy harvester for power generation, anchoring to the ground by the electrostatic adhesive feet. Combing three functions into one compact design yet using simple, lightweight structure and common materials can be counted as a breakthrough in both robotics and triboelectric nanogenerators, and such integration of TENG and electrostatic robot is unprecedented yet really promising. This is considered as the main novelty of this work.

More specifically, the integrated multifunctional system acts as the main body (or the actuation body) of a soft mobile robot. Two electroadhesive feet are used for anchoring when the robot works as a TENG or a vibration sensor. Besides, two pairs of (front and rear) directional-friction spines [22] have been used to facilitate the locomotion of the robot. For detailed studies, the electrostatic adhesion forces between the foot and the substrate (conductive) under different DC voltages are measured first. The electrostatic actuation body is then characterized for achieving larger extensions under amplitude-modulated voltage

actuation. The locomotion speeds of the robot under different working modes are compared next. Thereafter, the vibration energy harvesting performance of the robot or the TENG is investigated, and the relationship among the base vibration frequency, amplitude, and the electrical output is experimentally identified and numerically fitted. Subsequently, a trial of vibration sensing is shown. In the end, a demonstration of the robot for locomotion, vibration energy harvesting, and sensing is given.

2. Results

2.1. Structure and working mechanism

As shown in Fig. 1a and b, the robot mainly consists of an electrostatic actuation body and two feet. The actuation body includes two electrodes (spring steel, each is 50 μm in thickness, and 12.7 mm and 30 mm in width and length) which are aligned to overlap each other. These electrodes are covered by polyimide tape (55 μm in thickness and 15 mm and 32 mm in width and length, respectively) for insulation. With one end of the aligned electrodes stuck by the polyimide tape, and the other end of each electrode is connected to an electroadhesive foot by a compliant joint made of double-layered polyimide tape. The two electroadhesive feet are identical, and each of them mainly includes a copper electrode (7 μm in thickness and 15 mm and 35 mm in width and length) which is coated with a $BaTiO_3$ layer (which has a high dielectric constant [24] and thus large electroadhesive force, 30 μm in thickness) on one side and is attached with a PVC sheet (250 μm in thickness) on the other side for the backing. We attach four spines (made of bent spring steel wires) to the actuation body. These spines can generate directional friction, i.e., both the front and rear halves of the actuation body experience much smaller friction force from the ground in moving forward than backward. Due to the use of spines, the frictional contact pair can be dominated by the point-to-surface contact, which often results in much larger friction than the surface-to-surface contact when the normal force keeps unchanged. Since the contact area is relatively small in a point-to-surface contact, the surface roughness, within a certain range, may have a minor effect on the friction and thus have an insignificant influence on the movement of the robot. Nonetheless, the unveiling of the actual effect requires systematic experimental investigation, which is not a focus of this study. Undoubtedly, a too rough or too smooth surface may disable the movement function of the robot. Moreover, the robot can carry a tool for more functions. For example, by attaching a mini camera (weighs 1 g, 9.5 mm × 9.5 mm × 12 mm, model MC900, 3RDEE Co. Ltd) to the actuation body, the robot has the capability of visual sensing. The load (i.e., the camera) also works as a proof mass when the robot works in the energy harvesting and vibration sensing modes, which will be detailed in the following context. The maximum load of the robot was hard to decide since it involves not only the actuation capability of the body actuator but also the dynamics of the robot during movement, energy harvesting, and sensing, and the application frequency. Both energy harvesting and vibration sensing are dependent on the proof mass of the oscillation system or on the load of the robot. Different loads can result in distinct performance in both energy harvesting and vibration sensing. The mini camera (1 g) used here is heavier than typical commercial temperature-humidity sensors (e.g., the SENSIRION Model 3.000.465 weighs 0.015 g), capacitors (e.g., the Seiko CPX3225A752D weighs 0.024 g), and other possible loads. Hence its payload capacity is adequate for typical scenarios.

The locomotion of the robot is quite similar to that of an inchworm. At first, during the movement, with the potential difference between the two electrodes of the actuation body, the actuation body closes up owing to the electrostatic attractive force generated in between. Since electrostatic force is a short-range force, the relatively narrow gap at the top or the joint of the zipper-structure helps initiate the zipping which can then be spread to the relatively bigger gap [18]. Using such kind of zipping motion to directly actuate a robot (with its feet attached on the
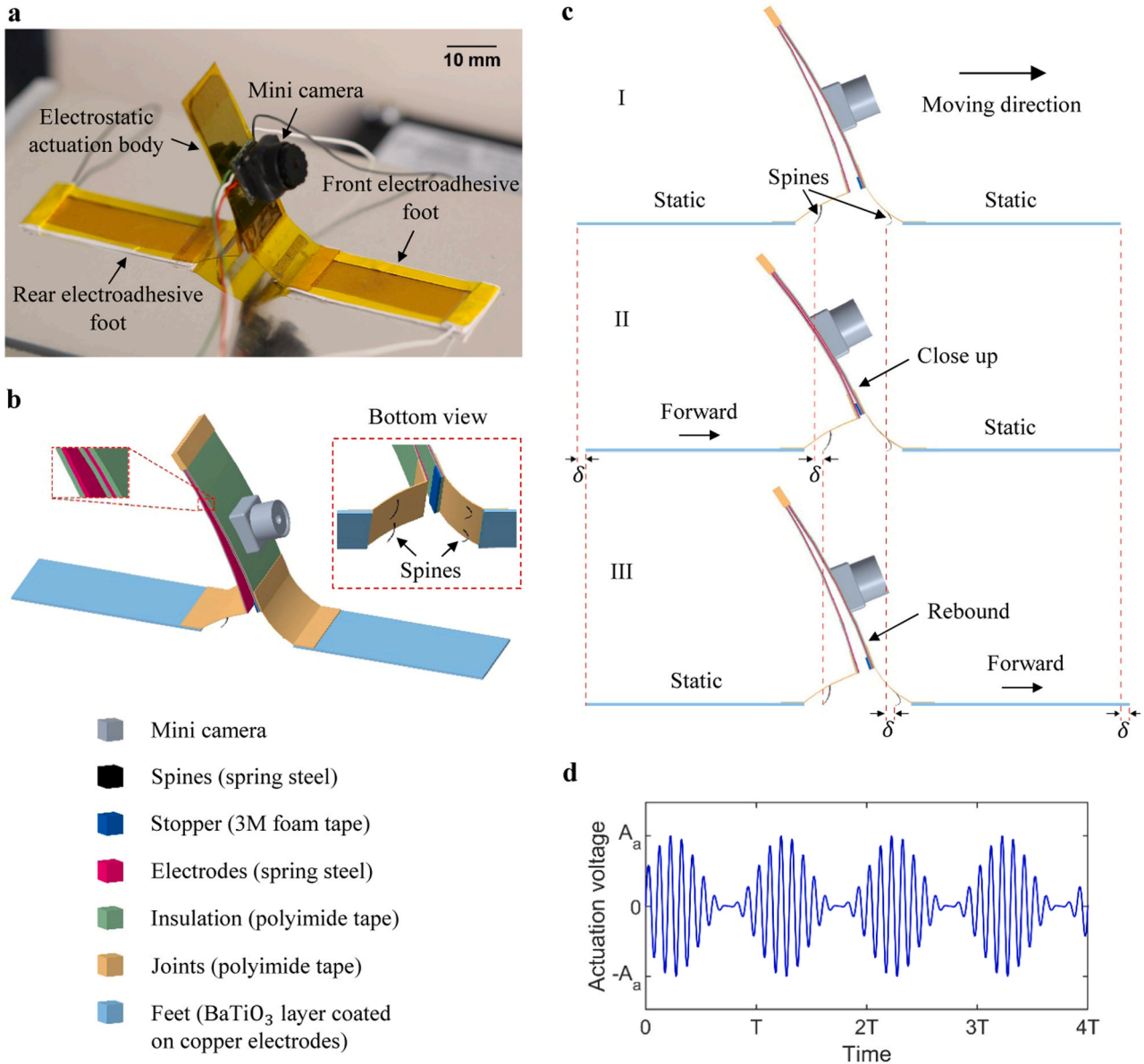
Fig. 1. Structure and working mechanism of the electrostatic robot. a. Photo of a prototype of the robot. b. Schematic diagram showing the structural details of the robot. c. Gait description of the robot. d. An example of the AM voltage used for actuation.

zipping electrodes), especially a soft one, is rare in literature. Due to the directional friction caused by the spines, the rear foot is dragged forward while the front foot remains static, as depicted in Fig. 1c. Then, by reducing the potential difference, the electrostatic attractive force is decreased and can no longer balance the restoring force generated by the elastic structure of the actuation body. As a result, the front foot of the robot is catapulted forward while the rear foot keeps still, as shown in Fig. 1c II and III, and then a new movement cycle starts. For actuation, the amplitude-modulated (AM) voltage is introduced as the actuation voltage since it can result in a larger extension compared to the sinusoidal voltage (more details are given in the following context), and it can be expressed as [25]:

$$V_{AM}(t) = (1 + m\sin(2\pi f_m t))A_c\sin(2\pi f_c t) \quad (1)$$

where $A_c\sin(2\pi f_c t)$ is the carrier waveform and A_c the amplitude and f_c the carrier frequency, f_m the modulation frequency, and m the modulation index and $m \geq 0$. An example of the AM voltage is given in Fig. 1d, where A_a is the amplitude of the actuation voltage.

When the robot moves to a place with vibration (e.g., in a gas turbine, jet engine, or pipeline), the robot can turn into the mode of energy harvesting or, more specifically, into a TENG, as shown in Fig. 2a, by removing the actuation voltage and applying DC voltages to the electroadhesive feet. The feet then electrostatically adhere onto the metal substrate (Fig. 2b) and the upper section of the actuation body oscillates freely along with the substrate. Note that sticking onto nonconductive substrates is still challenging for the proposed robot owing to the design of the foot electrodes. Although comb-like electrodes have been demonstrated to have better electrostatic adhesion performance, more attention has been given to the integration of TENG and electrostatic actuator in this work. Variable voltage can be generated from the electrodes of the actuation body owing to the contact electrification and electrostatic induction [8]. Fig. 2c shows the charge transfer process of the TENG during oscillation. After contact, the polyimide layer would gain negative charges while the electrodes obtain an equal amount of positive charges due to the fact that steel tends to lose electrons while polyimide is more likely to gain electrons according to the triboelectric series [8]. From step ① to ②, electrode I bends away from electrode II,
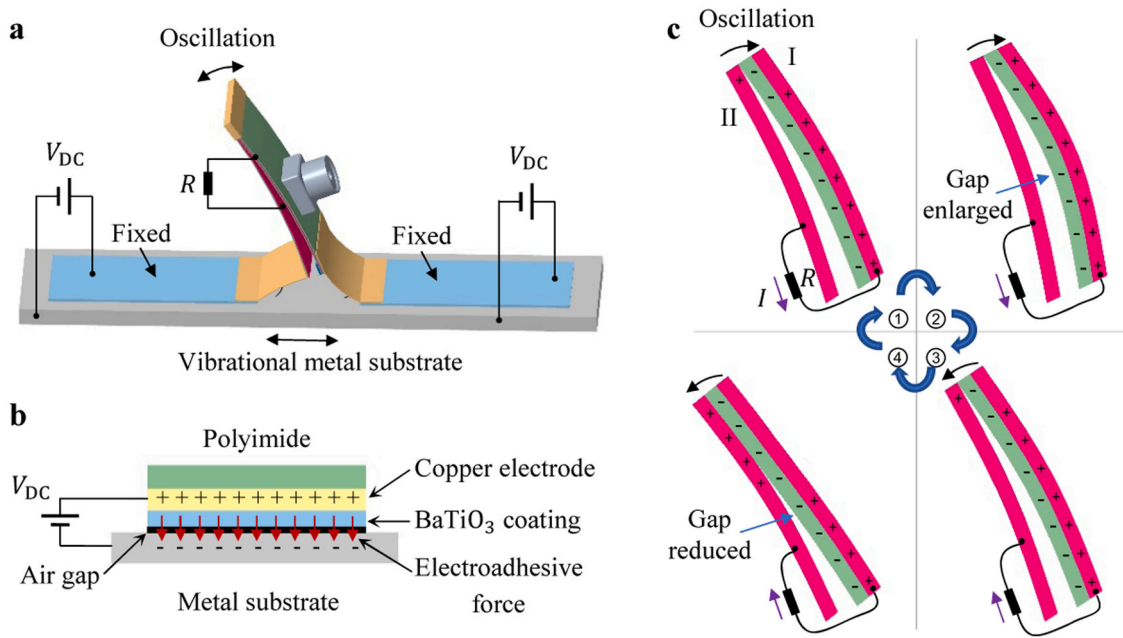
Fig. 2. Working mechanism when the robot works as a TENG. a. Schematic diagram showing the robot working as a TENG. b. Schematic diagram of the electrostatic adhesion between the foot and the metal substrate. c. Schematic diagram showing the charge transfer process and the oscillation of the TENG (or the actuation body).

which results in electrons flowing from electrode I to II and thus a reverse current flow. Then, electrode I approaches electrode II from step ② to ③, and the current flows from electrode I to II. Similarly, from step ③ to ④, more and more charges are inducted on electrode II. Afterwards, the TENG structures restore to the equilibrium position again from step ④ to ①, and the resulted current flows from electrode II to I. Hereto, a complete cycle has been fulfilled and the cycle begins anew.

The output of the TENG or the robot depends on the characteristics of the base vibration. Studying the energy harvesting performance of the TENG under different base vibrations will not only help the optimization work but also facilitate the establishment of the relationship between the output of the TENG and the characteristics of the base vibration (such as the vibration amplitude and frequency). Moreover, once such a relationship is known, vibration sensing can be done by analyzing the output of the robot which can then be regarded as the vibration signal acquired by the robot. More details and results will be revealed in the following context.

2.2. Characterization of the electroadhesive foot

When we supply the electrodes in the feet with high voltage, electrostatic adhesive force is generated between the electrodes and the conductive substrate, as shown in Fig. 2b, where the electrostatic force is perpendicular to the substrate. Considering that there can exist a thin air gap between the foot and the substrate, the normal adhesion force can then be expressed as [18]:

$$F_{\mathrm{N}} = \frac{\frac{1}{2}\varepsilon_{\mathrm{air}}\varepsilon_0 S V_{\mathrm{b}}^2}{\left(\frac{\varepsilon_{\mathrm{air}}}{\varepsilon_{\mathrm{ins}}}t_{\mathrm{ins}} + t_{\mathrm{air}}\right)^2} \qquad (2)$$

where ε_0 is the vacuum permittivity, $\varepsilon_{\mathrm{air}}$ and $\varepsilon_{\mathrm{ins}}$ the dielectric constants of the air and the insulator (BaTiO$_3$ coating), t_{air} and t_{ins} the thicknesses of the thin air gap and the insulator, S the area of the foot, and V_{b} the voltage between the foot and the substrate. According to Coulomb's law of friction, the tangential adhesion force can be given by:

$$F_{\mathrm{T}} = \mu_{\mathrm{e}}F_{\mathrm{N}} \qquad (3)$$

where μ_{e} is the coefficient of friction of the electroadhesive contact

between the foot and the substrate.

We measured the normal and tangential adhesive force exerted on the foot by pulling the foot vertically and horizontally, respectively, with the setup shown in Fig. S1. The typical loading curves of both cases are given in Fig. S2, and their peaks are taken as the measured value of each condition. By varying the applied DC voltage, the diagrams of adhesion forces against the voltage can be obtained and are shown in Fig. 3. At each condition, 5 trials are conducted. Both normal and tangential adhesion forces increase along with the increase of the DC voltage. Within the test range of the DC voltage, the maximal normal and tangential adhesion forces are 0.24 N and 0.47 N, respectively. As shown in Fig. 3, the simulation results show a good correlation with their experimental counterparts. The slight discrepancy might result from the unflatten of the electrode films of the foot. The parameter values in the simulation are given in Table S1, in which t_{air} is identified using the least square method. In the tests, the BaTiO$_3$ coating was likely to break down when the DC voltage was larger than 350 V. Thus, the voltage applied to the foot is capped at 300 V in the following study.

2.3. Characterization of the electrostatic actuation body

We measured the actuation body by the experimental setup shown in Fig. S3. During the tests, a DC voltage of 300 V was applied to the rear foot while the front foot was free to move under the excitation of the actuation body. A laser displacement sensor (Panasonic, HL-G105-A-C5) was used to measure the extension of the robot, and a small L-shaped plate, whose weight was negligible, was mounted on the front foot to reflect the laser beam for facilitating the measurement.

There are four parameters in the expression of the AM voltage as shown in Eq. (1). To simplify the study, it is assumed that the carrier frequency and the modulation frequency are proportional, $f_{\mathrm{c}}/f_{\mathrm{m}} = 10$. When the amplitude, carrier frequency, and modulation frequency are fixed at $A_{\mathrm{c}} = 1$ kV, $f_{\mathrm{c}} = 8$ Hz, and $f_{\mathrm{m}} = 0.8$ Hz, the vibration responses of the robot or the actuation body at different modulation indexes are acquired. The diagram of the extension or vibration amplitude of the robot versus the modulation index is presented. The extension at each value of the modulation index is averaged from the amplitudes of 96 periods (one period lasts $1/f_{\mathrm{m}}=1.25$ s). As shown in Fig. 4a, the extension of the robot increases linearly with the modulation index linear, because the
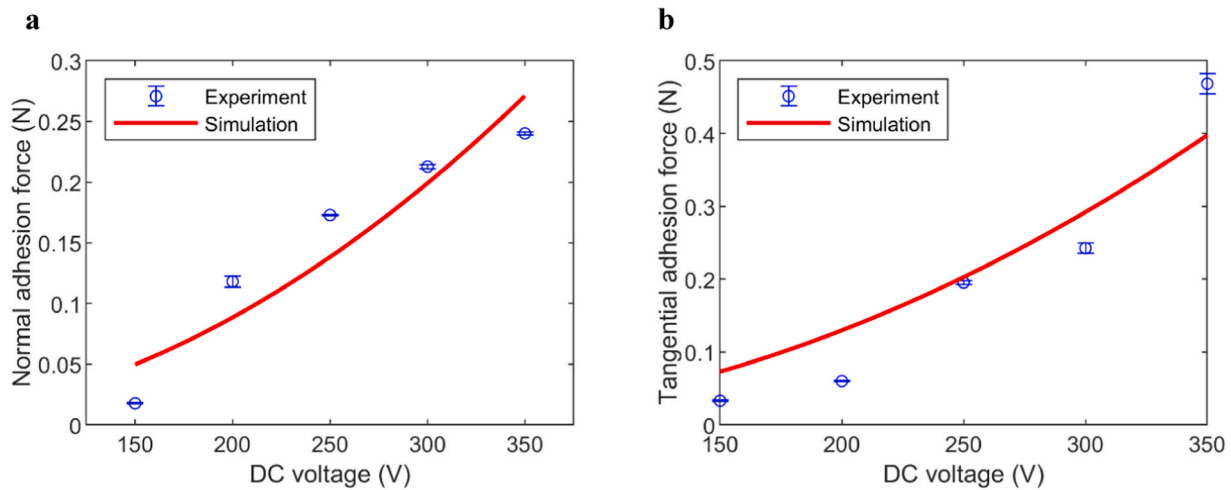
Fig. 3. Measured and simulated electroadhesive forces between the foot and the metal substrate at different DC voltages. a. Normal adhesion force versus DC voltage. b. Tangential adhesion force versus DC voltage.

modulation index directly contributes to the amplitude of the actuation voltage. Thus, for simplicity, the modulation index will be fixed at 1 in the following study. As shown in Fig. 4b, the carrier amplitude also increases the foot extension, with a nonlinear form. To figure out the effects of the carrier frequency, the extension of the robot has been measured at different frequencies with the amplitude fixed at $A_c = 0.8$ kV. As shown in Fig. 4c, the extension reaches the peak at 9 Hz (corresponding to the resonant frequency).

Then, the extension of the robot with the presence of a load (a micro camera) is studied using the same test rig. The diagram of the extension versus the carrier frequency is shown in Fig. 4d. In comparison with the case without a camera or with Fig. 4c, the resonant peak has been shifted towards a lower frequency and is around 5 Hz, which is mainly due to the increase of the total mass by involving the camera. Here, the oscillating system can be regarded as a mass-spring system. When the mass m is increased and the stiffness of the spring k is held fixed, the resonant or natural frequency $\omega_n = \sqrt{k/m}$ decreases, and thus the resonant peak appears at a lower frequency compared to the case without the camera. Besides, the extension has been reduced correspondingly. At the resonant frequency, i.e., $f_c = 5$ Hz, the extensions of the robot under the actuation of both the AM and the sinusoidal voltages (with amplitudes A_a and frequency f_c) at different actuation amplitudes are compared in Fig. 4e. A much larger extension is achieved under the AM actuation voltage compared to a sinusoidal actuation voltage. The relationship between the carrier amplitude A_c and the actuation amplitude A_a can be obtained through numerical calculation (A_a cannot be analytically derived from Eq. (1)) and turns out to be linear as shown in Fig. 4f. Besides, as shown in Fig. 4e, the extension reaches a steady value as the increase of the actuation amplitude, because the contact and separation motion or the vibro-impact motion of the actuation body has appeared at $A_a = 1.1926$ kV and thus the largest stroke of the robot has been achieved (Movie S1). The same phenomenon has also appeared when the robot is under sinusoidal actuation in which case, however, the front electrode or electrode I (Fig. 2c) of the actuation body has been confined to vibrate within a range which is closer to the rear electrode or electrode II, and thus resulting in much smaller extensions (Movie S2). This is because that the overall amplitude of the sinusoidal actuation is at a relatively large level and thus full rebound of the actuation body cannot be achieved (especially when it comes to relatively high frequency), whereas there are drops of the overall amplitude in the AM actuation and thus full rebound is allowed. Therefore, area b in Fig. 4f includes the amplitudes that can induce vibro-impact motion of the actuation body, while area a (shown in grey) comprises those who cannot.

Supplementary material related to this article can be found online at doi:10.1016/j.nanoen.2021.106368.

Supplementary material related to this article can be found online at doi:10.1016/j.nanoen.2021.106368.

2.4. The speed of the robot

To investigate the speed of the robot under different carrier frequencies, the carrier amplitude is set as $A_c = 1.2$ kV ($A_a = 2.385$ kV) and the carrier frequency is varied from 1 Hz to 15 Hz. At each frequency, the time for the robot to travel a distance of 30 mm was recorded as one sample, and five samples were used to calculate the average speed. As shown in Fig. 5a, the velocity reaches a flat peak of around 2.2 mm/s during the range from 5 to 10 Hz. We demonstrate the prototype traveling more than 30 mm during 14 s, as shown in Fig. 5b. It has been observed that the vibro-impact motion of the actuation body appears at 5 Hz and then disappears at 12 Hz as the increase of the carrier frequency, which results in the sudden increase and decrease of the speed at these two frequencies (Movie S3). Nonetheless, by mainly adjusting the carrier amplitude and frequency, the speed of the robot can be well controlled. Although the mobility of the robot is limited, and that is, currently, the robot can only move in a straight line, the study of such an integrated, multifunctional robot is merely at an early stage, and it is intended to demonstrate the design, the multifunctionality, and the compatibility (between the electrostatic actuator and the triboelectric nanogenerator) in this work. To increase the freedom of moving, a direct way is using a parallel assembly of the current robot. The assembled robot may be in an H shape, such as the dielectric elastomer actuated (DEA) wall-climbing robot in Ref. [26]. In that case, the heading can be changed by steering. Alternatively, the electrostatic actuator in the middle of the robot can be made by a special origami structure which allows partial electrostatic adhesion, for example leaving one side open while clamping the other side (the present zipper-like actuator clamps at both sides when voltage is applied). This idea is similar to the one used in Ref. [27]. Nonetheless, the preference for a future work will be given to the origami design since it has the potential in not only enabling steering but also enhancing electrostatic actuation and energy harvesting.

Supplementary material related to this article can be found online at doi:10.1016/j.nanoen.2021.106368.

Here we refer the case with only the actuation body working (without the electrostatic adhesion) as the OA mode, and both the actuation body and feet supplied with voltage as the BF mode. In addition to the AM voltage applied to the actuation body, two rectangular voltage waves of different phases ($\varphi = [\pi/2 \quad 3\pi/2]$) with an
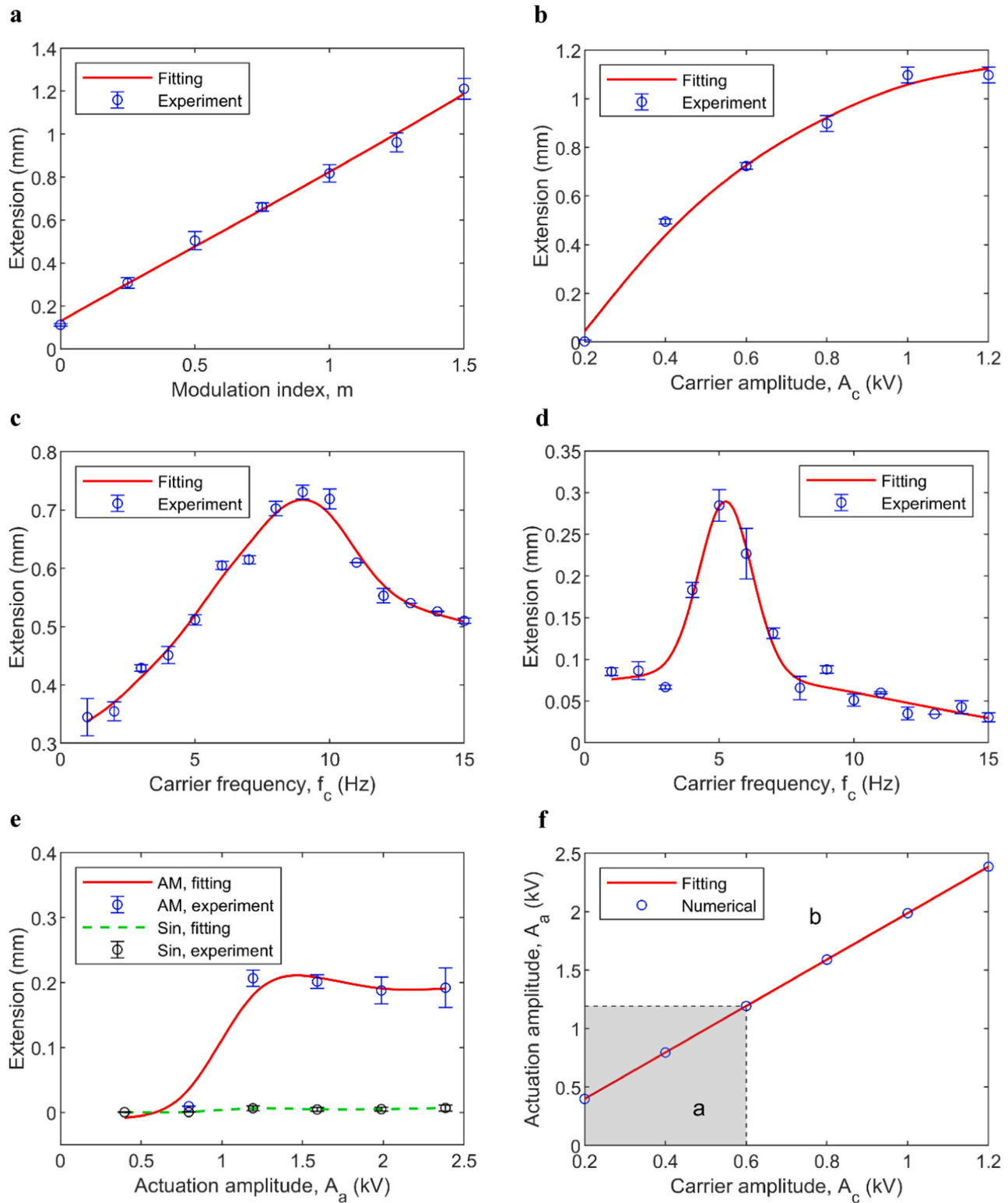
Fig. 4. Characterization of the actuation body. a. Influences of the modulation index *m* on the extension of the robot with the camera absent. b. Influences of the carrier amplitude A_c on the extension with the camera absent. c. Effects of the carrier frequency f_c on the extension with the camera absent. d. Effects of the carrier frequency f_c on the extension with camera present. e. Effects of the actuation amplitude A_a on the extension with camera present and the comparison between the performances of AM and sinusoidal actuation voltages. f. The relationship between the carrier amplitude A_c and the actuation amplitude A_a.

amplitude of V_r are applied to the front and the rear electroadhesive feet (BF mode). An example of the voltage waves is given in Fig. 5c in which the duty cycle of the rectangular waves *D* is 50%. The duty cycle is the ratio of the time that the DC voltage is on to the period of the rectangular

wave. If not otherwise specified, the following values of parameters, i.e., $A_c = 1.2$ kV, $f_c = 5$ Hz, and $V_r = 250$ V, are used in the study below. It has been found that the robot can barely move when the duty cycle of the rectangular voltage is 50%. The speed of the robot increases along
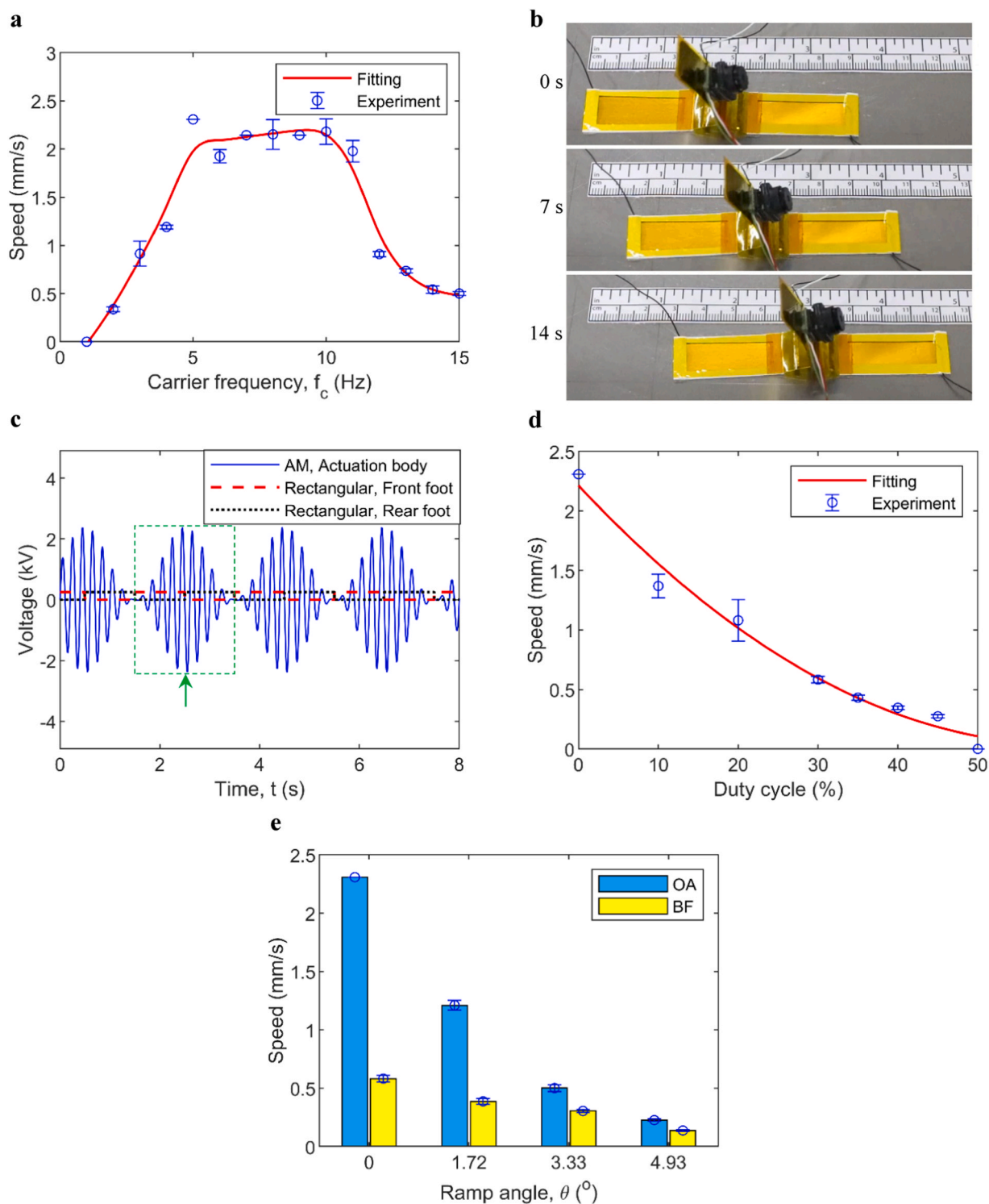
Fig. 5. The speed of the robot. a. The speed of the robot at different carrier frequencies under the mode with only the actuation body working (the OA mode). b. An image sequence of the locomotion of the robot under the OA mode when the carrier frequency is 5 Hz. c. An example of the voltage waves under the mode with both the electroadhesive feet and the actuation body working (the BF mode, the green dashed rectangle circles a complete actuation period and the green arrow marks the half period). d. The speed of the robot at different duty cycles under the BF mode. e. A bar chart showing the climbing results and the comparison between the OA and the BF modes.

with the decrease of the duty cycle, as shown in Fig. 5d, due to the working mechanism of the actuation body. There are a number of voltage peaks and troughs in an actuation period, as shown in Fig. 5c. Each peak or trough theoretically corresponds to a closing of the actuation body (some obvious closings can be observed at relatively high peaks or deep troughs from the local view of the locomotion at 5 Hz in

Movie S3). In the first half actuation period (the left half of the green dashed rectangle), the front foot is electrostatically fixed, while the rear foot is free to move and oscillates alternately forward and backward along with the oscillation of the rear electrode (electrode II). At the end of the first half actuation period (which is marked by the green arrow in Fig. 5c), the rear foot returns to its initial position with zero net

displacement. As a result, there is no locomotion of the robot within the first half actuation period. A similar situation exists in the second half actuation period (the right half of the green dashed rectangle) which also ends without any locomotion. However, with the decrease of the duty cycle, there would be a time interval, over which both feet are free to move (zero DC voltages are applied on them) and the robot is able to achieve locomotion but less efficiently, within each half actuation period, and the larger the time interval or the smaller the duty cycle, the

higher the speed. Therefore, when the duty cycle equals zero, there are no DC voltages applied on the feet, and the robot moves fastest.

To test the climbing ability, the robot is placed on an angle-adjustable ramp (Fig. S4). The speed of the robot is measured under the above two actuation modes: the OA mode and the BF mode (with a duty cycle of 30%). The results are presented in the form of a bar chart in Fig. 5e. Certainly, the speed of the robot decreases against the increase of the ramp angle in both cases, and the speed under the OA mode is
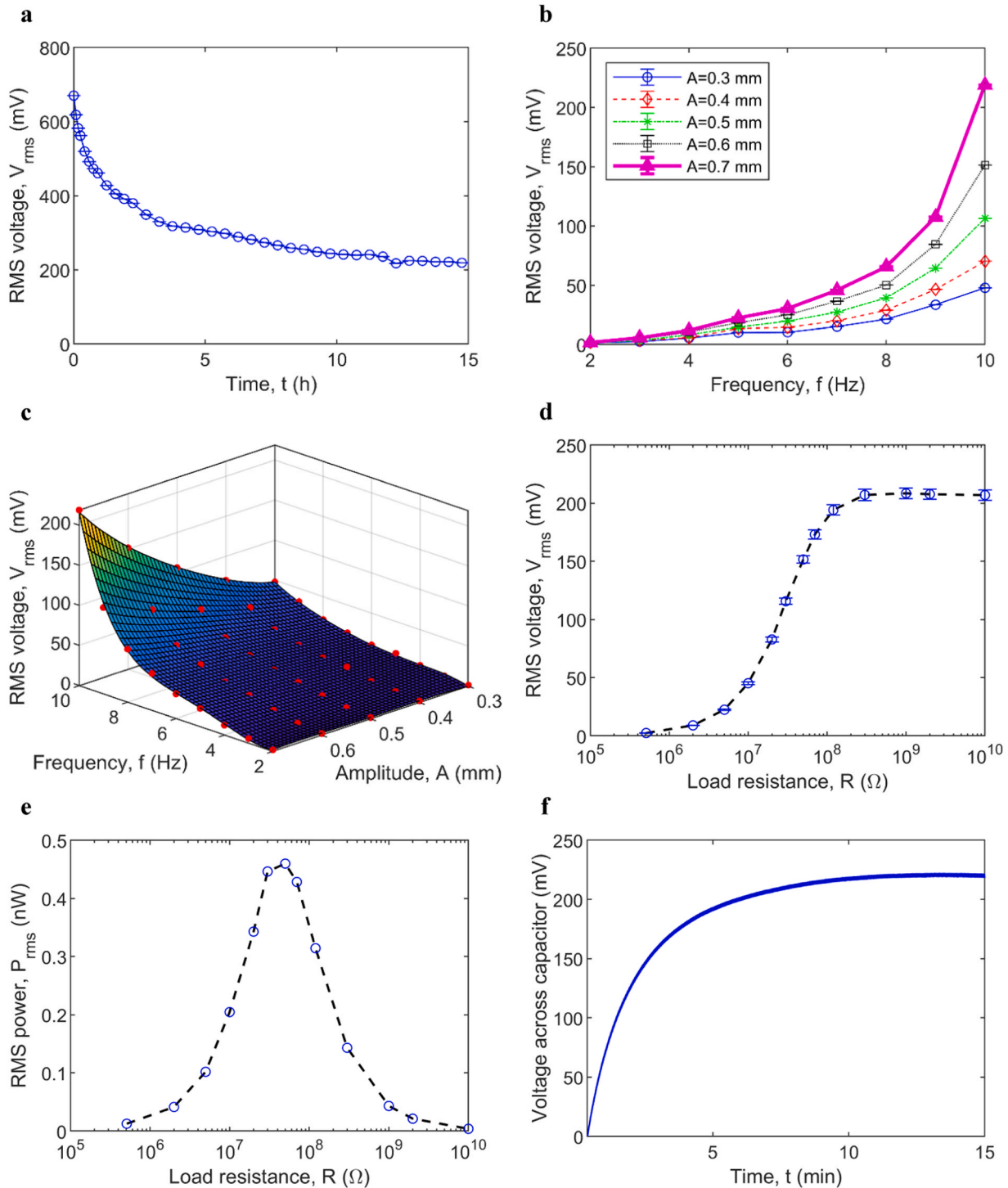

Fig. 6. Vibration energy harvesting of the robot. a. The decaying of the harvested RMS voltage. b. Effects of the base excitation frequency and amplitude on the RMS voltage output of the robot. c. A fitting of the relationship among the excitation frequency, the excitation amplitude and the RMS voltage. d. Effects of the load resistance on the RMS voltage. e. The RMS power output calculated with the mean value of RMS voltages. f. The voltage across a capacitor (1 μF, 50 V) during charging.

larger than that under the BF mode. The steepest ramp that the robot can climb is around 5 degrees (Movie S4). Both the results of the duty cycle test and the climbing test suggest the adoption of the OA mode rather than the BF mode. The surrounding environment in practical applications can be complex, and 5-degree climbing ability may not be sufficient. The climbing ability of the proposed robot mainly relies on its electrostatic actuator. Currently, a zipper-like structure is used for both the electrostatic actuator and the TENG, though an origami structure or a superposition of the current structure may provide stronger actuation and then better climbing ability. Owing to the simple zipper-like structure, the relationship between the electrical output of the TENG and the base vibration can be well identified, which greatly facilitates vibration sensing. Thus, a trade-off has been made here. Nevertheless, electrostatic actuators of origami structures will be developed in the future study.

Supplementary material related to this article can be found online at doi:10.1016/j.nanoen.2021.106368.

2.5. Vibration energy harvesting

During the locomotion of the robot, the electrostatic actuation body converts electrical energy into mechanical energy through the electrostatic effect, and if such an electrostatic effect can be named as the inverse electrostatic effect (similar to the nomenclature of the direct and inverse piezoelectric effects [28]), then TENGs employ the direct electrostatic effect to transform mechanical energy into electrical energy. Hence, the robot uses the inverse electrostatic effect during locomotion while employs the direct electrostatic effect during vibration energy harvesting as well as vibration sensing.

Assuming the base excitation (or the vibration of the substrate) is sinusoidal in the horizontal direction. The experimental setup, which is used to investigate the effects of the excitation frequency and amplitude on vibration energy harvesting, is shown in Fig. S5, and the corresponding schematic diagram is the same as Fig. 2a. Under the base excitation, the robot has its both feet electrostatically anchored onto a sinusoidal vibration platform, and the actuation body works as a TENG, which converts the vibrational energy into electrical energy.

However, when the robot moves to the designated place (vibrational) and shifts from the locomotion mode to the vibration energy harvesting mode, the actuation voltage used in the former mode could affect the electrical output generated in the latter mode, possibly through the charge residue. It has been found that the electrical output of the robot experiences a decaying before becoming steady when the measurement starts just after the shift, and the corresponding results (f = 10 Hz, A = 0.7 mm) are shown in Fig. 6a where the root-mean-square (RMS) voltage is the RMS value of the open-circuit voltage and is averaged from 500 excitation periods. The results indicate that the electrical output needs around 15 h to become steady. The time histories of the harvested voltage at the start and the end of decaying are given in Fig. S6. After the decaying, the effects of the excitation frequency and amplitude on the RMS voltage are investigated and are shown in Fig. 6b. It can be seen that the RMS voltage increases with the increase of both the excitation frequency and amplitude. At f = 10 Hz and A = 0.7 mm, the RMS voltage reaches the highest value and is about 219 mV. To figure out the relationship between the excitation frequency, the excitation amplitude, and the RMS voltage output, Fig. 6b is regenerated in a 3D parametric space, as shown in Fig. 6c, where the surface is a fitting of the experimental data shown in red dots. The fitted surface can then represent the relationship and be used for the identification of the base vibration. More details of the method will be given in the next section.

To investigate the effects of the load resistance on the electrical output of the robot and to figure out the optimal load resistance at where the power output of the robot reaches the highest, a resistor is connected to the TENG, and its value is varied from 100 kΩ to 10 GΩ when the robot is under the base excitation of f = 10 Hz and A = 0.7 mm. The mean values of the RMS voltage against the load resistance are given in

Fig. 6d. Obviously, the RMS voltage increases as the increase of the load resistance, but it eventually reaches a relatively steady value. The corresponding diagram of the RMS power versus load resistance is shown in Fig. 6e, and, apparently, the RMS power output of the robot reaches the highest value of around 0.46 nW at R = 50 MΩ, which is low and certainly cannot be used for real-time powering the camera or the actuator. Given the small dimensions, it is not easy to improve the power output which is usually highly dependent on the effective contact area in TENGs. However, by accumulating the harvested energy in a capacitor, some low-consumption sensors, which are not necessarily for real-time continuous sensing, can be powered. Besides, by electrostatically anchoring the robot, i.e., applying 300 VDC to both feet, the power consumption of the robot is around 0.1 mW (details are shown in Fig. S8 and Table S2). Although the harvested power is less than the consumed power, the vibration sensing function (which is based on the vibration energy harvesting function and will be shown in the following section) of the robot is not affected at all, and the robot can be regarded as a moveable vibration sensor of low-power consumption. Therefore, the energy harvesting of such scale is still useful.

Although the power output of the robot is relatively small, it can still be used to power some low-consumption sensors and it is worth mentioning that the low-power output does not affect the performance of the robot in vibration sensing. Here, the robot is used to charge a capacitor (1 μF, 50 V, the circuit used is depicted in Fig. S7) under the base excitation of f = 10 Hz and A = 0.7 mm, and the charging curve is shown in Fig. 6f in which the voltage across the capacitor gradually increases up to 222 mV in around 13 mins.

2.6. Vibration sensing

To utilize the obtained relationship among the vibration frequency, the vibration amplitude and the RMS voltage output of the robot for vibration identification, the RMS voltage can be obtained from the output of the robot first, and then the vibration frequency of the base or the substrate can be identified by spectrum analysis of the voltage output of the robot. Since two of the three parameters (f, V_{rms}, and A) are known, the third parameter, i.e., the vibration amplitude A, can be calculated through numerical interpolation by utilizing the obtained relationship. Therefore, the robot can work as a vibration energy harvester and as a vibration sensor for environmental vibration monitoring.

The accuracy of the vibration identification through the robot has been tested at 16 points which are selected from the frequency-amplitude parametric plane. The points cover four nominal frequencies (f = 3 Hz, 5 Hz, 7 Hz, and 9 Hz), and each nominal frequency is related to four nominal amplitudes (A = 0.35 mm, 0.45 mm, 0.55 mm, and 0.65 mm). At each nominal frequency, the spectrum analysis has been carried out for the voltage outputs of the robot under four nominal amplitudes. The spectrum diagrams at these four nominal frequencies are shown in Fig. 7. It can be seen that the identified frequencies (which correspond to the spikes) match the nominal frequencies pretty well at these 16 points. These results indicate that the electrical output of the robot perfectly inherits the frequency characteristics of the base vibration, which greatly facilitates the vibration sensing. The effective sensing range of the vibration frequency is from 2 Hz to 10 Hz, which matches the frequency range of the vibrations of civil infrastructures (0.3–10 Hz) [29] pretty well. To expand the range, the structural stiffness and the load of the robot can be adjusted accordingly, since both of them affect the dynamical response of the robot to the base vibration.

With the obtained RMS voltage and the identified vibration frequency, the vibration amplitude can be interpolated from the relationship. The relative error between the identified amplitude and the nominal amplitude is calculated to show the accuracy, and the results of the same nominal amplitude but different frequencies are compared in each subfigure in Fig. 8. It can be seen that the relative errors are all
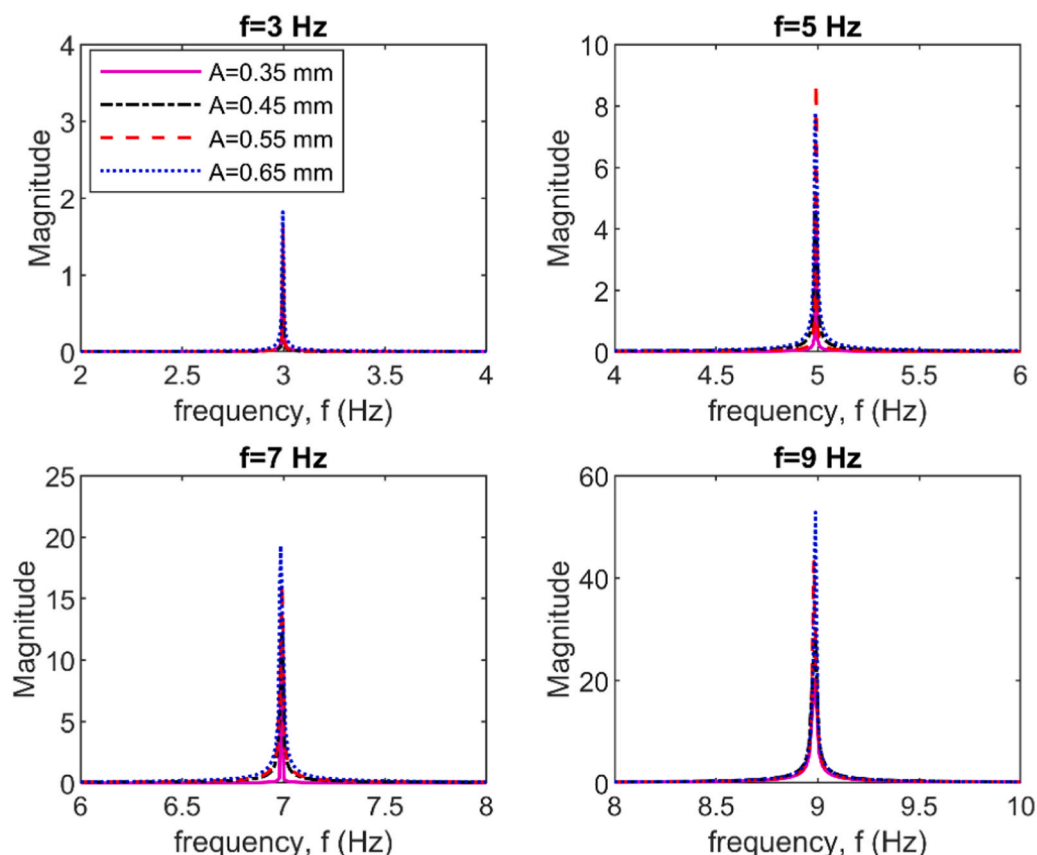
Fig. 7. Spectrum diagrams of the voltage output of the robot showing the identified frequencies (which correspond to the spikes, the nominal frequency is titled at the top of each subfigure) at different amplitudes.

below 16% except at $A = 0.35$ mm, $f = 3$ Hz, and their average value is 8.7%. Besides, the relative errors at higher frequencies are smaller than those at lower frequencies and are below 11%. Considering that TENGs can be sensitive to temperature, humidity, etc., such accuracy is acceptable. To further improve the sensing accuracy of the vibration amplitude, an H-shaped design that has two such robots connected in parallel (thus has two electrical outputs) might be helpful, and the sensing error might be reduced by averaging these two electrical outputs. Nevertheless, the accurate identification of the vibration frequency can still make the robot competent at moveable vibration sensing, especially for applications where the monitoring of the vibration frequency matters, such as monitoring structural vibrations that are close to resonant frequencies.

2.7. Demonstration

In this section, a demonstration is shown to further elucidate the working mechanisms of the robot. The schematic diagrams of the experimental setups and the working mechanisms are shown in Fig. 9a. The robot is actuated by applying AM voltage to the actuation body, and then it moves from Table 1 to the designated place, i.e., table 2, during which period the mini camera monitors the surrounding environment, such as recording the information shown ahead of its path. When the robot arrives at the designated place or table 2, the AM actuation voltage is switched off, and the actuation body is connected to an energy harvesting circuit. Both feet of the robot are electrostatically anchored on table 2 by applying DC voltages between the feet and the table. Then, table 2 starts to vibrate, and the actuation body works as a TENG to harvest the mechanical energy, and the harvested steady voltage is used for vibration sensing by employing the method proposed in previous sections. Fig. 9b shows the image sequence of the locomotion of the

robot from Table 1 to 2 and the corresponding camera views (the information board is vertically placed in front of the robot and is not shown in the figure), from a far point to a near point. The robot is then electrostatically anchored on table 2 (aluminum), which can vibrate sinusoidally at a certain frequency and amplitude for vibration energy harvesting and sensing, and an example of the time history of the harvested steady voltage is given at the bottom right corner in Fig. 9b. More details of the demonstration, including a flowchart of the vibration identification process, are shown in Movie S5.

Supplementary material related to this article can be found online at doi:10.1016/j.nanoen.2021.106368.

3. Conclusion and discussion

In summary, a multifunctional robotic system capable of locomotion, vibration energy harvesting and sensing is proposed in this paper. The robotic system mainly consists of the main body for actuation as an actuator and for energy conversion and vibration sensing as a TENG. It also includes two electroadhesive feet for electrostatic anchoring, spines for directional friction, and a mini camera (which could also be other functional modules) for monitoring the surrounding environment. Since the electrostatic robot utilizes the inverse electrostatic effect during locomotion, i.e., converting electrical energy (control voltage) into mechanical energy (movement of the robot), and uses the direct electrostatic effect during vibration energy harvesting, i.e., converting mechanical energy (vibration of the surrounding environment) into electrical energy (voltage output of the robot), the proposed robot might be, to the best knowledge of the authors, the first robotic application that integrates both direct and inverse electrostatic effects in literature. Such a fascinating integration can be really promising and sets a good example for integrating TENGs and robots. By using certain designs, a
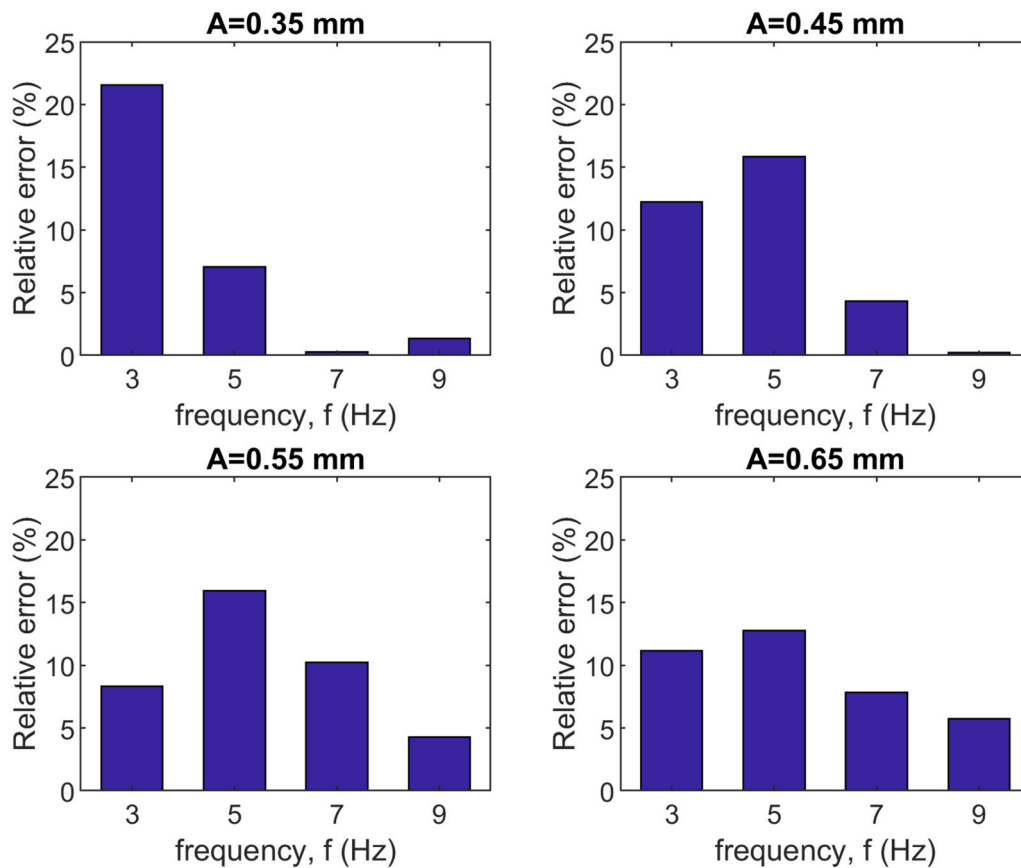
Fig. 8. Relative errors between the identified amplitude and the nominal amplitude (titled at the top of each subfigure) at different frequencies.

TENG can completely change its role to work as an electrostatic actuator or robot, which should be the first of its kind in TENGs. Moreover, the actuation body of the robot is also an integration of both an actuator and a sensor, and such an integration is structurally realized by using only two electrodes and a dielectric in between, which is much superior to the conventional robots that employ independent actuators and sensors. In addition, there is a potential to enable self-powered electronics (such as low-consumption sensors) since the robot can work as an energy converter, which can be fascinating. Note that self-powering is not necessarily meant to get the whole system self-powered. To the proposed robotic system and to many other electrostatic robotics, self-powering of the entire system is difficult since electrostatic robotics usually require high voltage (kV) for electrostatic actuation but need low voltage (V) for powering sensors. Thus, partially self-powering can still be helpful. Other merits of the proposed robot include: structural simplicity as it can be handcrafted, which is a major advantage over some electrostatic robots that have machined comb-like electrodes [19,30], easy control as it is only controlled using voltages and cost effective as the materials used are cheap.

Specifically, the resonant frequency, where the extension reaches the largest value, of the robot can be tuned by the attached payload, such as a mini camera, which allows more freedom in design. In comparison between the actuation voltage waveforms, the robot has a much larger extension, which then corresponds to a much higher speed under the amplitude-modulated (AM) voltage than that under the sinusoidal voltage of the same actuation amplitude. Under the AM voltage actuation and with the increase of the actuation frequency, the speed of the robot experiences a sudden increase as the vibro-impact motion of the actuation body appears at 5 Hz and then suffers an abrupt drop as the vibro-impact motion disappears at 11 Hz. Within the range from 5 Hz to 11 Hz, the speed of the robot is the highest and is around 2.2 mm/s. In addition to the AM voltage applied to the actuation body, by applying

rectangular voltages to both of the electroadhesive feet, the robot can also move under the cooperation between the actuation body and the adhesion feet (similar to the working mechanism shown in Ref. [26]) but in a lower speed than that only under the AM voltage actuation or only with the operation of the actuation body. The climbing test shows that the robot can climb a ramp of 5 degrees of incline. It is the potential to enhance the climbing ability by stacking several pairs of the actuation body (similar to the origami configuration shown in Ref. [20]) to increase the stroke of the robot.

When the robot shifts into the vibration energy harvesting mode from the locomotion mode, the electrical output of the robot will experience a decaying period of around 15 h before becoming steady, and this decaying is mainly due to the charge residue caused by the actuation voltage. The highest steady value of the RMS voltage output is about 219 mV, which can charge a capacitor of 1 μF and 50 V up to 222 mV in around 13 mins, under the base vibration of $f = 10$ Hz and $A = 0.7$ mm. At a load resistance of around 50 MΩ, the RMS power output of the robot reaches the highest value of around 0.46 nW. The relationship among the vibration frequency, the vibration amplitude and the RMS voltage output of the robot is experimentally identified and numerically fitted. The spectrum analysis of the harvested voltage provides a perfect identification of the vibration frequency. The vibration amplitude is interpolated from the relationship, and the relative error between the identified and the nominal vibration amplitudes is mostly below 16% and has an average value of 8.7%, which can be satisfying.

A comparison of some centimeter-scale crawling robots is given in Table 1. Despite the low crawling speed of the proposed robot, it is still comparable to some other types of crawling robots. In particular, the multifunctionality of the proposed robot is achieved without employing any external function modules, which is a distinguishing characteristic. Nevertheless, future work might consider the improvements of the electroadhesive foot and the electrostatic actuation body. The comb-like
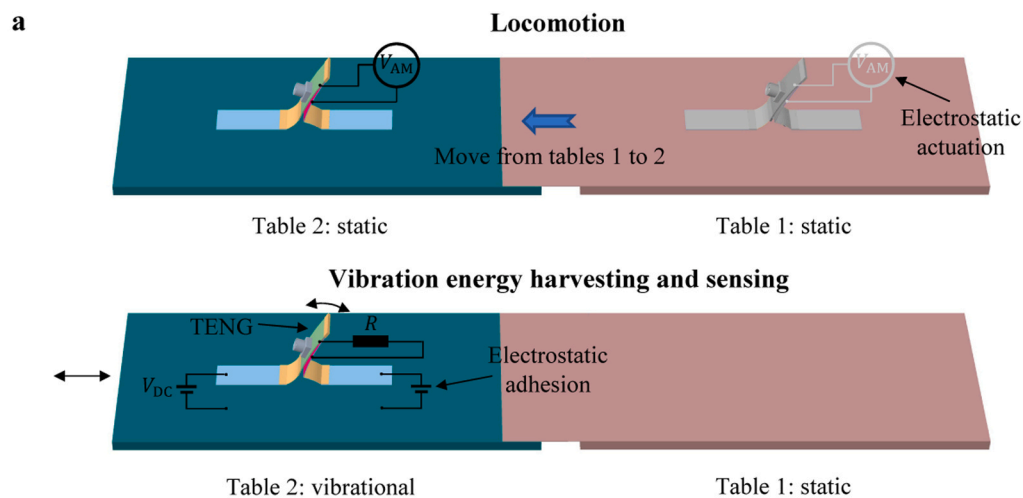
Fig. 9. Demonstration of the robot for locomotion and vibration energy harvesting and sensing. a Schematic diagrams showing the working mechanisms. b Image sequences of the locomotion of the robot to the designated place, i.e., table 2, and the camera view showing the recorded information, i.e., "CUHK" and "SUSTech" and their corresponding Chinese names (the information board is vertically placed in front of the robot), and a photo of the robot on the vibrational table 2 for vibration energy harvesting and sensing (at bottom left corner, blue downward pointing arrows mean electrostatically anchored and other arrows indicate oscillations) and an example of the time history of the harvested steady voltage (at bottom right corner).
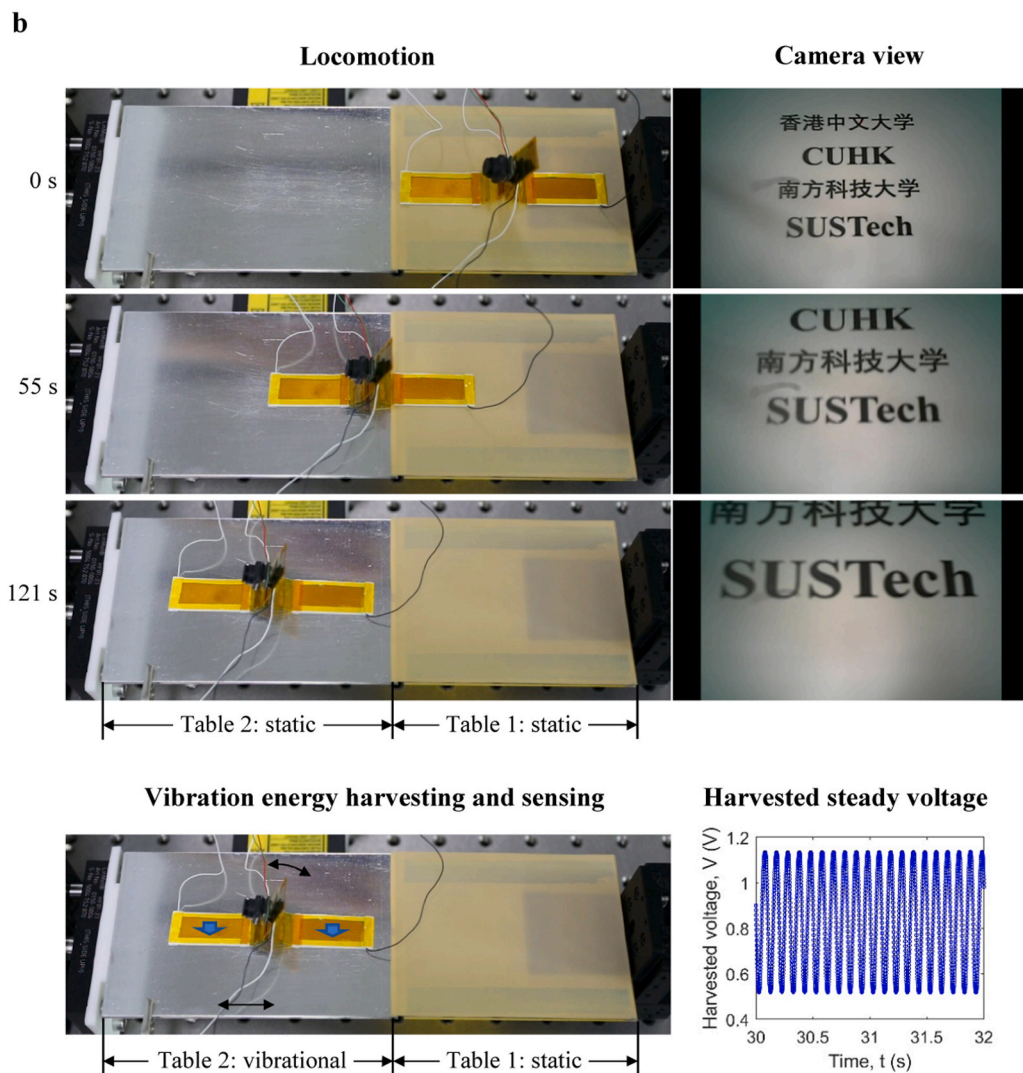
electrode [19,30] may be employed by the foot to cope with non-conductive bases, which allows the robot to work on different materials and thus broadens the practical applications. The use of an origami electrostatic actuation body similar to Ref. [20] can probably generate larger actuation force or locomotion speed, enhance vibration energy harvesting performance and enable the steering function.

Besides, for multidirectional energy harvesting and vibration sensing, an origami design can be useful as well, though an alternative might be to tailor the robot for vibrations along a specific direction. In addition, new materials and manufacturing techniques that help reduce the charge residue and thus the decaying period can also be a great contribution. In all, the developed multifunctional robotic system may enable moveable

Table 1

Comparison of centimeter-scale crawling robots (PZT: Piezoelectric actuator, SMA: shape-memory actuator, DEA: Dielectric elastomer actuator, HA: Hygroscopic actuator, and EA: Electrostatic actuator).

Actuator	Speed (mm/s)	Robot length (mm)	Weight (g)	Multifunctional without external modules
PZT [31]	3.2	20	1.4	No
SMA [32]	30	30	2.4	No
SMA [33]	0.57	110	29	No
DEA [34]	1.1	51	N/A	No
DEA [26]	88.46	85	N/A	No
HA [35]	6	25	0.035	No
EA [21]	40	75	0.45	No
EA (**This work**)	2.2	91	2.46	3-in-1: Electrostatic actuation, vibration energy harvesting, and vibration sensing

sensing and energy harvesting, with potential applications in structural health monitoring, environmental surveillance, rescue, risky intervention, etc.

4. Materials and methods

4.1. Materials and fabrication

The robot mainly comprises polyimide tape, spring steel, copper foil and $BaTiO_3$ paste. Both the electrodes of the actuation body and the spines were cut from the spring steel sheet (50 μm in thickness, H+S). Each joint of the robot was made by sticking two identical polyimide tape (55 μm in thickness, DuPont) together with both the non-sticky sides left outside, and both ends of the formed double-layer polyimide tape were folded to shape into the origami profile shown in Fig. 1c. The spines were fashioned into directional-friction formations and were attached onto the joints using double-sided tape. To fabricate the electroadhesive foot, a $BaTiO_3$ paste (DuPont, 8153) was uniformly painted on a copper foil (7 μm in thickness) first, and the painted copper foil was then cured at 140 °C for 1 h in an infrared drying coating machine (MSK-AFA-ES200). Next, a cut-to-size PVC backing sheet (250 μm in thickness) was wrapped by the $BaTiO_3$-coated (30 μm in thickness) copper electrode with the coating left outside, and the top was covered by the polyimide tape for electrical insulation as well as packaging. The prepared actuation body and electroadhesive feet were then assembled by the joints, i.e., by sticking one folded end of a joint to the actuation body and the other to the electroadhesive feet.

4.2. Control and data acquisition platforms

The control signals, including the AM actuation voltage applied to the actuation body and the rectangular voltage or the DC voltage applied to the electroadhesive feet, were generated in LabVIEW first, and the generated digital signal was then converted to analog signal by an analogy output module (NI, PXIe 6738). High voltage amplifiers (Trek, model 615–3) were finally used to amplify the analogy output. For the data acquisition, two modules (NI, TB4330 and NI, TB4309) were used to log the data acquired, respectively, by a load cell (Panasonic, LSB 200 50 g) and a laser displacement sensor (Panasonic, HL-G105-A-C5).

4.3. Measurement of the electroadhesion force

As the experimental setups shown in Fig. S1, a tension testing machine (ZHIQU, ZQ990B) was employed to pull the foot and a load cell (Panasonic, LSB 200 50 g) was connected in between to measure the tension force, and a data acquisition board (NI, TB4330) was used to log the data. Since the foot was relatively soft, two 3D printed backing sheets (which were relatively rigid and had negligible masses) were, respectively, attached to the foot in both normal and tangential adhesion

force measurements, and a string was used to connect the backing sheet and the load cell. Before the measurement, a DC voltage was applied between the foot and the substrate (aluminum). The loading curve was recorded as the tension machine pulling the foot, and its peak was considered as the measured value of the adhesion force. The DC voltage was varied to different values and five tests were carried out at each value to obtain the average adhesion force.

4.4. Measurement of the extension

The rear foot of the robot was electrostatically anchored onto the substrate (aluminum) by applying a DC voltage of 300 V in between, and the vibration of the robot under the AM voltage actuation was measured by a laser displacement sensor (Panasonic, HL-G105-A-C5), as shown in Fig. S3. The extension was then averaged from the vibration amplitudes of certain number of periods.

4.5. Vibration energy harvesting measurement

In the experiments, an aluminum platform was driven by a linear motor (LinMot, P01–23 × 160) which was programmed (by LinMot Talk) for sinusoidal excitations. A laser displacement sensor (Panasonic, HL-G105-A-C5) was used to monitor the vibration of the platform. The robot was stuck onto the platform by applying DC voltages (300 V) to both of the electroadhesive feet. Under the base excitation, the electrical output of the TENG or the robot was measured using an electrometer (Keithley, 6514).

and Innovation Commission of Shenzhen Municipality (ZDSYS20200811143601004). The authors acknowledge the assistance of SUSTech Core Research Facilities.

Appendix A. Supporting information

Supplementary data associated with this article can be found in the online version at doi:10.1016/j.nanoen.2021.106368.

References

[1] M.M. Rathore, A. Ahmad, A. Paul, S. Rho, Urban planning and building smart cities based on the Internet of Things using Big Data analytics, Comput. Netw. 101 (2016) 63–80, https://doi.org/10.1016/j.comnet.2015.12.023.

[2] F. Yildiz, Potential ambient energy-harvesting sources and techniques, J. Technol. Stud. 35 (2009) 40–48. ⟨http://10.0.82.69/jots.v35i1.a.6⟩.

[3] A.R.M. Siddique, S. Mahmud, B. Van Heyst, A comprehensive review on vibration based micro power generators using electromagnetic and piezoelectric transducer mechanisms, Energy Convers. Manag. 106 (2015) 728–747, https://doi.org/10.1016/j.enconman.2015.09.071.

[4] C. Falconi, Piezoelectric nanotransducers, Nano Energy 59 (2019) 730–744, https://doi.org/10.1016/j.nanoen.2019.03.027.

[5] G. Gautschi, Piezoelectric Sensorics, Springer, Berlin, Heidelberg, 2002, https://doi.org/10.1007/978-3-662-04732-3.

[6] Z.L. Wang, T. Jiang, L. Xu, Toward the blue energy dream by triboelectric nanogenerator networks, Nano Energy 39 (2017) 9–23, https://doi.org/10.1016/j.nanoen.2017.06.035.

[7] A. Toprak, O. Tigli, Piezoelectric energy harvesting: state-of-the-art and challenges, Appl. Phys. Rev. 1 (2014), 031104, https://doi.org/10.1063/1.4896166.

[8] Z.L. Wang, L. Lin, J. Chen, S. Niu, Y. Zi, Triboelectric Nanogenerators, Springer, 2016.

[9] Y. Bai, L. Xu, C. He, L. Zhu, X. Yang, T. Jiang, J. Nie, W. Zhong, Z.L. Wang, High-performance triboelectric nanogenerators for self-powered, in-situ and real-time water quality mapping, Nano Energy 66 (2019), 104117, https://doi.org/10.1016/j.nanoen.2019.104117.

[10] H. Yang, Y. Pang, T. Bu, W. Liu, J. Luo, D. Jiang, C. Zhang, Z.L. Wang, Triboelectric micromotors actuated by ultralow frequency mechanical stimuli, Nat. Commun. 10 (2019) 1–7, https://doi.org/10.1038/s41467-019-10298-7.

[11] S. Wang, L. Lin, Z.L. Wang, Triboelectric nanogenerators as self-powered active sensors, Nano Energy 11 (2015) 436–462, https://doi.org/10.1016/j.nanoen.2014.10.034.

[12] C. Wu, T.W. Kim, J.H. Park, B. Koo, S. Sung, J. Shao, C. Zhang, Z.L. Wang, Self-powered tactile sensor with learning and memory, ACS Nano 14 (2019) 1390–1398, https://doi.org/10.1021/acsnano.9b07165.

[13] C. Wu, A.C. Wang, W. Ding, H. Guo, Z.L. Wang, Triboelectric nanogenerator: a foundation of the energy for the new era, Adv. Energy Mater. 9 (2019), 1802906, https://doi.org/10.1002/aenm.201802906.

[14] W. Sun, B. Li, F. Zhang, C. Fang, Y. Lu, X. Gao, C. Cao, G. Chen, C. Zhang, Z.L. Wang, TENG-Bot: triboelectric nanogenerator powered soft robot made of uni-directional dielectric elastomer, Nano Energy 85 (2021), 106012, https://doi.org/10.1016/j.nanoen.2021.106012.

[15] T. Bu, H. Yang, W. Liu, Y. Pang, C. Zhang, Z.L. Wang, Triboelectric effect-driven liquid metal actuators, Soft Robot 6 (2019) 664–670, https://doi.org/10.1089/soro.2018.0161.

[16] R. Legtenberg, J. Gilbert, S.D. Senturia, M. Elwenspoek, Electrostatic curved electrode actuators, J. Micro Syst. 6 (1997) 257–265, https://doi.org/10.1109/84.623115.

[17] J.D. Grade, H. Jerman, T.W. Kenny, Design of large deflection electrostatic actuators, J. Micro Syst. 12 (2003) 335–343, https://doi.org/10.1109/JMEMS.2003.811750.

[18] M. Taghavi, T. Helps, J. Rossiter, Electro-ribbon actuators and electro-origami robots, Sci. Robot. 3 (2018), https://doi.org/10.1126/scirobotics.aau9795.

[19] H. Wang , A. Yamamoto , A thin electroadhesive robot driven by an electrostatic film actuator for inspection in a narrow gap, in: 2013 IEEE Int. Symp. Safety, Secur. Rescue Robot., IEEE, 2013: pp. 1–6. https://doi.org/10.1109/SSRR.2013.6719335.

[20] J. Li, H. Godaba, Z.Q. Zhang, C.C. Foo, J. Zhu, A soft active origami robot, Extrem. Mech. Lett. 24 (2018) 30–37, https://doi.org/10.1016/j.eml.2018.08.004.

[21] C. Jin, J. Zhang, Z. Xu, I. Trase, S. Huang, L. Dong, Z. Liu, S.E. Usherwood, J.X.J. Zhang, Z. Chen, Tunable, flexible, and resilient robots driven by an electrostatic actuator, Adv. Intell. Syst. 2 (2020), 1900162, https://doi.org/10.1002/aisy.201900162.

[22] H. Wang, P. York, Y. Chen, S. Russo, T. Ranzani, C. Walsh, R.J. Wood, Thermoresponsive hemostatic hydrogel with a biomimetic nanostructure constructed from aggregated collagen nanofibers, Biomacromolecules 22 (2021) 319–329, https://doi.org/10.1177/02783649211002545.

[23] C. Naresh, P.S.C. Bose, C.S.P. Rao, Shape memory alloys: a state of art review, in: IOP Conf. Ser. Mater. Sci. Eng., IOP Publishing, 2016: p. 12054. https://doi.org/10.1088/1757–899X/149/1/012054.

[24] T. Tsurumi, H. Adachi, H. Kakemoto, S. Wada, Y. Mizuno, H. Chazono, H. Kishi, Dielectric properties of BaTiO3-based ceramics under high electric field, Jpn. J. Appl. Phys. 41 (2002) 6929–6933, https://doi.org/10.1143/JJAP.41.6929.

[25] M.E. Van Valkenburg, W.M. Middleton, Reference Data for Engineers: Radio, Electronics, Computers and Communications, Elsevier, 2001.

[26] G. Gu, J. Zou, R. Zhao, X. Zhao, X. Zhu, Soft wall-climbing robots, Sci. Robot. 3 (2018), https://doi.org/10.1126/scirobotics.aat2874.

[27] J. Cao, L. Qin, J. Liu, Q. Ren, C.C. Foo, H. Wang, H.P. Lee, J. Zhu, Untethered soft robot capable of stable locomotion using soft electrostatic actuation, Extrem. Mech. Lett. 21 (2018) 9–16, https://doi.org/10.1016/j.eml.2018.02.004.

[28] C.Q. Chen, Y.P. Shen, Three-dimensional analysis for the free vibration of finite-length orthotropic piezoelectric circular cylindrical shells, J. Vib. Acoust. Trans. ASME 120 (1998) 194–198, https://doi.org/10.1115/1.2893804.

[29] P.V. Malaji, S.F. Ali, Analysis of energy harvesting from multiple pendulums with and without mechanical coupling, Eur. Phys. J. Spec. Top. 224 (2015) 2823–2838, https://doi.org/10.1140/epjst/e2015-02591-7.

[30] H. Wang, A. Yamamoto, T. Higuchi, A crawler climbing robot integrating electroadhesion and electrostatic actuation, Int. J. Adv. Robot. Syst. 11 (2014) 191, https://doi.org/10.5772/59118.

[31] D. Lee , S. Kim , Y. Park , R.J. Wood , Design of centimeter-scale inchworm robots with bidirectional claws, in: 2011 IEEE Int. Conf. Robot. Autom., 2011: pp. 3197–3204. https://doi.org/10.1109/ICRA.2011.5980458.

[32] A.M. Hoover , E. Steltz , R.S. Fearing , RoACH: An autonomous 2.4g crawling hexapod robot, in: 2008 IEEE/RSJ Int. Conf. Intell. Robot. Syst., 2008: pp. 26–33. https://doi.org/10.1109/IROS.2008.4651149.

[33] S.-K. Lee, B. Kim, Design parametric study based fabrication and evaluation of in-pipe moving mechanism using shape memory alloy actuators, J. Mech. Sci. Technol. 22 (2008) 96–102, https://doi.org/10.1007/s12206-007-1011-z.

[34] S. Shian, K. Bertoldi, D.R. Clarke, Use of aligned fibers to enhance the performance of dielectric elastomer inchworm robots, in: Proc.SPIE, 2015. https://doi.org/10.1117/12.2084140.

[35] B. Shin, J. Ha, M. Lee, K. Park, G.H. Park, T.H. Choi, K.-J. Cho, H.-Y. Kim, Hygrobot: a self-locomotive ratcheted actuator powered by environmental humidity, Sci. Robot. 3 (2018) eaar2629, https://doi.org/10.1126/scirobotics.aar2629.